

## Microensing of Quasar UV Iron Emission

E. GUERRAS<sup>1,2</sup>, E. MEDIAVILLA<sup>1,2</sup>, J. JIMENEZ-VICENTE<sup>3,4</sup>, C.S. KOCHANEK<sup>5</sup>, J. A. MUÑOZ<sup>6</sup>, E. FALCO<sup>7</sup>, V. MOTTA<sup>8</sup>

### ABSTRACT

We measure the differential microensing of the UV Fe II and Fe III emission line blends between 14 quasar image pairs in 13 gravitational lenses. We find that the UV iron emission is strongly microensed in 4 cases with amplitudes comparable to that of the continuum. Statistically modeling the magnifications we infer a typical size of  $r_s \sim 4\sqrt{M/M_\odot}$  light-days for the Fe line emitting regions which is comparable to the size of the region generating the UV continuum ( $\sim 5 - 8$  light-days). This may indicate that a significant part of the UV Fe II and Fe III emission originates in the quasar accretion disk.

*Subject headings:* gravitational lensing: micro, quasars: emission lines

### 1. Introduction

Iron, the stable end product of nucleosynthesis, has a large number of electronic levels, generating thousands of emission line transitions distributed throughout the UV and optical

---

<sup>1</sup>Instituto de Astrofísica de Canarias, Vía Láctea S/N, La Laguna 38200, Tenerife, Spain

<sup>2</sup>Departamento de Astrofísica, Universidad de la Laguna, La Laguna 38200, Tenerife, Spain

<sup>3</sup>Departamento de Física Teórica y del Cosmos, Universidad de Granada, Campus de Fuentenueva, 18071 Granada, Spain

<sup>4</sup>Instituto Carlos I de importancia Física Teórica y Computacional, Universidad de Granada, 18071 Granada, Spain

<sup>5</sup>Department of Astronomy and the Center for Cosmology and Astroparticle Physics, The Ohio State University, 4055 McPherson Lab, 140 West 18th Avenue, Columbus, OH, 43221

<sup>6</sup>Departamento de Astronomía y Astrofísica, Universidad de Valencia, 46100 Burjassot, Valencia, Spain.

<sup>7</sup>Center for Astrophysics, 60 Garden Street, Cambridge, MA 02138, USA

<sup>8</sup>Departamento de Física y Astronomía, Universidad de Valparaíso, Avda. Gran Bretaña 1111, Valparaíso, Chile

that likely makes Fe II the main emission line contributor to the overall spectra of quasars and AGN. Statistical studies of quasar spectra find that variations between them are dominated by the relative strength of the Fe II emission (Boroson & Green 1992). In spite of the relevance of the iron lines to understanding the physics of AGN, both the mechanism generating the Fe II emission (Ferland et al. 2009), and the spatial scale of the region where it is emitted (Barth et al. 2013) are poorly understood. Two bands of Fe II emission are usually studied (see e.g. Baldwin et al. 2004): the UV pseudo-continuum between C III] $\lambda$ 1909 and Mg II] $\lambda$ 2798 and the optical blends in the H $\gamma$ -H $\beta$  region. The few reverberation mapping studies of Fe II indicate that the region emitting the UV Fe II lines (Maoz et al. 1993) is considerably smaller than the region emitting the optical Fe II lines (Kuehn 2008, Barth et al. 2013).

The size of the region generating the broad emission lines (BEL) in quasars can be also inferred from the impact of microlensing on the BEL. In a multiply imaged quasar, the magnification of each image of the quasar varies with time due to lensing by the stars in the lens galaxy (see the review by Wambsganss 2006). The dependence of the microlensing magnification on the size of the emission region has been used to estimate the size of different quasar regions including the accretion disk (see, e.g. Pooley et al. 2007, Morgan et al. 2010, Blackburne et al. 2011, Jiménez-Vicente et al. 2012), the Broad Line Region (BLR) (Abajas et al. 2007, Sluse et al. 2012, Motta et al. 2012, Guerras et al. 2013) and the non-thermal X-Ray emission region (Pooley et al. 2007; Morgan et al. 2008, 2012; Chartas et al. 2009; Dai et al. 2010; Blackburne et al. 2011; Mosquera et al. 2013). In the particular case of the iron emission lines, Sluse et al. (2007) analyzed spectra of RXS J1131–1231 and found that a large fraction of the optical Fe II emission arises in the outer parts of the BLR, although they also found evidence of a very compact region associated with Fe II.

Here we study the microlensing of the UV iron emission in a sample of 14 pairs of lensed quasar images, combining the spectra compiled by Mediavilla et al. (2009) with new observations. In Section 2, we describe the data and the procedure used to isolate the Fe II and Fe III line emission from the continuum and to then measure its microlensing. In Section 3, we use the measured microlensing amplitudes to derive constraints on the size of the UV iron emitting region and we discuss and summarize the results in Section 4.

## 2. Data Analysis

We started with the sample compiled by Mediavilla et al. (2009) and then added unpublished archival spectra taken with the VLT or the MMT, as summarized in Table 1. We focus on the wavelength region between the C III] $\lambda$ 1909 and Mg II] $\lambda$ 2798 emission

lines and we will use these lines to define a flux ratio baseline that is only weakly affected by microlensing (Mediavilla et al. 2009, 2011a, Guerras et al. 2013). Table 2 defines the wavelength regions we consider. We loosely follow the definition of the Fe II wavelength windows by Francis et al. (1991). The primary modification is that we do not include the regions around C III]λ1909 to avoid modeling the blended emission. Iron emission is split into two windows designated Fe(1), dominated by Fe III, and Fe(2), dominated by Fe II (Vestergaard & Wilkes 2001), each bracketed by line-free continuum regions (Kuraszkiewicz et al. 2002, Francis et al. 1991, Brotherton et al. 2001). Fe(1) corresponds to 2050-2115Å and Fe(2) corresponds to three regions: 2250-2320Å, 2333-2445Å, and 2470-2625Å.

We first fit 4 straight lines to the continuum regions bracketing the Fe emission windows (plus a continuum region bluewards of the C III]λ1909 line and other redwards of the Mg IIλ2798 line) and subtract it from the spectrum. Then, for each image-pair we normalize the continuum subtracted spectra to match the core of the Mg IIλ2798 emission lines defined by the total flux within  $\pm$  FWHM/2 of the line center. Provided these low ionization lines are only weakly affected by microlensing, as we found in Guerras et al. (2013), the normalization constant (that is, the ratio between the Mg IIλ2798 emission lines) gives us the intrinsic macrolens magnification between the images. The flux ratio of the continuum as compared to that of the Mg IIλ2798 emission lines then gives us an estimate of the continuum microlensing magnification:

$$\Delta m_{\text{cont}} = (m_1 - m_2)_{\text{cont}} - (m_1 - m_2)_{\text{MgII}\lambda 2798}. \quad (1)$$

In Figure 1, the superposition of the continuum subtracted and normalized (to the Mg IIλ2798 emission line) spectra are shown for each image-pair. The average SDSS quasar spectrum (Vanden Berk et al. 2001), continuum-subtracted following the same procedures, is shown for comparison. In all cases (except SBS 0909+532 and SDSS J1353+1138) the Mg IIλ2798 based normalization also matched the C III]λ1909 emission lines well, which shows that the continuum subtraction procedure has worked well and that there are no significant effects due to differential atmospheric refraction or slit misalignments. The exceptions were SBS 0909+532 which is strongly affected by differential extinction in the lens galaxy (Motta et al. 2002, Mediavilla et al. 2005, Mediavilla et al. 2011b) and, at a lower level, SDSS J1353+1138. Assuming that the differences in normalization between the C III]λ1909 and the Mg IIλ2798 emission lines in these two objects arise from extinction we have applied a linear extinction correction to match both emission lines simultaneously.

Examining Figure 1, we see significant differences between the spectra in the region between C III]λ1909 and Mg IIλ2798 in 4 cases: SDSS J0806+2006AB, FBQS J0951+2635AB, QSO 0957+561AB and SDSS J1353+1138. For each pair of images, 1 and 2, we can estimate

the microlensing in the two Fe regions by comparing the differential flux ratios between the iron blends and the Mg II $\lambda$ 2798 line that sets the baseline for no microlensing magnification. For example, we define

$$\Delta m_{\text{Fe}(1)} = (m_1 - m_2)_{\text{Fe}(1)} - (m_1 - m_2)_{\text{MgII}\lambda 2798}, \quad (2)$$

for region Fe(1) and similarly  $\Delta m_{\text{Fe}(2)}$  for region Fe(2). The same analysis can be performed using C III] $\lambda$ 1909 as the unmicrolensed baseline. For C III] $\lambda$ 1909 the definition of the continuum below the line is less well defined than for Mg II $\lambda$ 2798, so these results should be treated with more caution. Using the C III] $\lambda$ 1909 line we can, then, define estimates of the microlensing amplitudes  $\Delta m'_{\text{cont}}$ ,  $\Delta m'_{\text{Fe}(1)}$ , and  $\Delta m'_{\text{Fe}(2)}$ . All the resulting microlensing estimates are presented in Tables 3 and 4. In Figure 2 we compare the microlensing magnification estimates for the continuum underlying each line or blend, C III] $\lambda$ 1909, Mg II $\lambda$ 2798, Fe(1) and Fe(2), finding very good linear covariances. The Pearson correlation coefficients are above 0.95 in all cases, with two-tailed p-values well under 0.01. In the same Figures we also compare the microlensing measured in the Fe(1) and Fe(2) regions with the microlensing of the continuum regions adjacent to the C III] $\lambda$ 1909 and Mg II $\lambda$ 2798 emission lines. We find that the Fe(1) region has a significant correlation with the continuum, while the Fe(2) region does not.

### 3. Constraining the Size of the UV Iron Emission Line Region

We follow the procedure we used in Guerras et al. (2013) to estimate the size of the emission regions corresponding to Fe(1), Fe(2) and the continuum regions adjacent to the Mg II $\lambda$ 2798 and C III] $\lambda$ 1909 emission lines. We start by computing microlensing magnification maps using the inverse polygon mapping technique (Mediavilla et al. 2006, Mediavilla et al. 2011a). We take the dimensionless surface density,  $\kappa$ , and shear,  $\gamma$ , for each image from the lens models by Mediavilla et al. (2009) and Mediavilla et al. (2011). We assume a mass fraction in stars of 5% (Abajas et al. 2007, Mediavilla et al. 2006, Pooley et al. 2009, 2012) and a stellar mass of  $M = 1M_{\odot}$ . We generate microlensing magnification maps with an outer scale of 1100 lt-day and with a pixel scale of 0.04 Einstein radii (equal to 0.6 light-days in the worst case). Each magnification map is unit normalized and convolved with a Gaussian of size,  $r_s$ ,  $I \propto \exp(-R^2/2r_s^2)$  to model the source. We consider a linear (logarithmic) grid of sizes from  $r_s = 1.5$  to 13 lt-day with steps  $\Delta r_s = 0.5$  lt-day ( $\Delta \log_{10} r_s = 0.0408$ ). The probability of observing a magnitude difference  $\Delta m_{\text{obs},k}$  for image pair  $k$  ( $k = 1, \dots, 14$ ) given a source size  $r_s$  is then

$$p_k(\Delta m_{obs,k}|r_s) \propto \int f_{r_s,k,1}(m_1) f_{r_s,k,2}(m_1 - \Delta m_{obs,k}) dm_1 \quad (3)$$

where  $f_{r_s,k,1}(m)$  and  $f_{r_s,k,2}(m)$  are the frequency histograms obtained from the convolved magnification maps for images 1 and 2 (of pair  $k$ ), respectively. The joint likelihood for all the image pairs,

$$L(\Delta m_{obs,1}, \dots, \Delta m_{obs,14}|r_s) = \prod_{k=1}^{14} p_k(\Delta m_{obs,k}|r_s), \quad (4)$$

then gives the likelihood distribution for the size  $r_s$ .

Normalizing the likelihood functions to unity gives the Bayesian posterior probabilities with either a uniform (linear grid) or logarithmic (log grid) prior on  $r_s$ . Figures 3 and 4 show, for linear and logarithmic grids respectively, the resulting probability distributions for Fe(1), Fe(2), and the continuum under the Mg II  $\lambda$ 2798 (C III]  $\lambda$ 1909) line when using the Mg II  $\lambda$ 2798 (C III]  $\lambda$ 1909) line to estimate the flux ratios in the absence of microlensing. The most significant result is that the UV iron blends seem to originate in a region of size comparable to that of the underlying UV continuum. From these posterior probability distributions we obtain size estimates, in  $\sqrt{M/M_\odot}$  light-day units, for the uniform (logarithmic) prior of  $r_s = 8.1 \pm 4.1$  ( $r_s = 5.7 \pm 3.7$ ) and  $r_s = 7.6 \pm 3.8$  ( $r_s = 5.3 \pm 3.3$ ) for the Mg II  $\lambda$ 2798 and C III]  $\lambda$ 1909 continua, respectively, in reasonable agreement with current expectations about the size of the region generating the continuum in quasars (e.g. Morgan et al. 2010, Jimenez-Vicente et al. 2012). Note that the redder (relative to C III]  $\lambda$ 1909) Mg II  $\lambda$ 2798 continuum region is larger, as expected from a disk that is hotter towards its center. We obtain similar sizes, in  $\sqrt{M/M_\odot}$  light-day units, for the Fe(1) and Fe(2) emission regions with  $r_s = 5.0 \pm 2.5$  ( $r_s = 5.4 \pm 2.4$ ) and  $r_s = 5.6 \pm 2.9$  ( $r_s = 4.6 \pm 2.6$ ), using the Mg II  $\lambda$ 2798 lines as the magnification reference and  $r_s = 3.3 \pm 1.5$  ( $r_s = 3.2 \pm 1.3$ ) and  $r_s = 3.9 \pm 1.8$  ( $r_s = 3.4 \pm 1.5$ ), using C III]  $\lambda$ 1909. While the C III]  $\lambda$ 1909 estimates are systematically smaller, the results are statistically consistent.

#### 4. Discussion and Conclusions

We have found evidence that the UV iron pseudo-continuum regions are microlensed, with an amplitude comparable to that of nearby continuum emission regions. When we formally estimate the size we find  $r_s \sim 4\sqrt{M/M_\odot}$  light-days, somewhat smaller than the continuum regions ( $r_s \sim 5 - 8\sqrt{M/M_\odot}$  light-days) and far smaller than either the high or low ionization line emission regions in the BLR as estimated either with microlensing

(Guerras et al. 2013) or reverberation mapping (see e.g. Zu et al. 2011). These quantitative results should be regarded as preliminary since the sample is small and a single object (SDSS J1353+1138) has a disproportionate impact on the size estimates. In any case, our estimate for the size is in reasonable agreement with the results for the UV Fe II emission region based in reverberation mapping by Maoz et al. (1993). Other reverberation map studies indicate that the Fe II optical emission lines arise from a substantially larger region (Kuehn 2008, Barth et al. 2013). However, Sluse et al. (2007) also found that a part of the optical Fe II emission may originate in a more compact region.

It is also interesting to explore the shape of the spectra to know whether microlensing acts selectively over some components of the pseudo-continuum and may shed light on the structure and kinematics of the inner regions of quasars. The shape of the unmicrolensed spectra resembles the average SDSS quasar spectra well (see Figure 1). The microlensed spectra, however, seem to be selectively enhanced at some of the spectral features in the iron emission templates from Vestergaard & Wilkes (2001). This is particularly true for the Fe(1) blend that appears strongly magnified in 3 of the 4 microlensed objects. On the other hand, in the Fe(2) blend of SDSS J1353+1138 (see also the low S/N spectra from FBQS J0951+2635 and SDSS J0806+2006), the enhanced features look broader and more flat-topped. Notice, in particular, the relative weakness of the C II] $\lambda$ 2326 emission line compared to the unmicrolensed spectra and the strong enhancement of the Fe II emission at  $\sim 2300\text{\AA}$  that can be hardly identified in the average SDSS quasar spectrum. A similar relative enhancement of the Fe II emission around the (tentatively identified) Fe III] $\lambda$ 2418 (narrow)+[Ne IV] $\lambda$ 2423 blend is observed in SDSS J0806+2006. High S/N ratio spectra combined with detailed modeling of the iron emission could help to understand both the origin of the iron emission and the structure of the innermost regions of quasars (inner BLR or/and accretion disk).

In a series of papers we have used archival spectra of lensed quasars and microlensing to measure the fraction of matter in compact objects (Mediavilla et al. 2009), the size of quasars accretion disk (Mediavilla et al. 2011a, Jimenez-Vicente et al. 2012), the size of the BLR (Guerras et al. 2013) and the temperature profile of the quasars accretion disk (Jimenez-Vicente et al. 2013). It is clear that the next step is to revisit these objects to search for spectral changes, or even to begin systematic spectroscopic monitoring.

This research was supported by the Spanish Ministerio de Educación y Ciencia with the grants AYA2010-21741-C03-01/02. J.J.V. is also supported by the Junta de Andalucía through the FQM-108 project. J.A.M. is also supported by the Generalitat Valenciana with the grant PROMETEO/2009/64. C.S.K. is supported by NSF grant AST-1009756. V.M. gratefully acknowledges support from FONDECYT through grant 1120741.

## REFERENCES

- Abajas, C., Mediavilla, E., Muñoz, J. A., Gómez-Álvarez, P., & Gil-Merino, R. 2007, *ApJ*, 658, 748
- Baldwin, J. A., Ferland, G. J., Korista, K. T., Hamann, F., & LaCluyzé, A. 2004, *ApJ*, 615, 610
- Barth, A. J., Pancoast, A., Bennert, V. N., et al. 2013, *ApJ*, 769, 128
- Blackburne, J. A., Pooley, D., Rappaport, S., & Schechter, P. L. 2011, *ApJ*, 729, 34
- Boroson, T. A., & Green, R. F. 1992, *ApJS*, 80, 109
- Brotherton, M. S., Tran, H. D., Becker, R. H., Gregg, M. D., & Laurent-Muehleisen, S. A., White, R. L., 2001, *ApJ*, 546, 775
- Chartas, G., Kochanek, C. S., Dai, X., Poindexter, S., & Garmire, G. 2009, *ApJ*, 693, 174
- Dai, X., Kochanek, C. S., Chartas, G., et al. 2010, *ApJ*, 709, 278
- Ferland, G. J., Hu, C., Wang, J.-M., et al. 2009, *ApJ*, 707, L82
- Francis, P. J., Hewett, P. C., Foltz, C. B., Chaffee, F. H., Weymann, R. J. & Morris, S. L., 1991 *ApJ*, 373, 465
- Guerras, E., Mediavilla, E., Jimenez-Vicente, J., et al. 2013, *ApJ*, 764, 160
- Jiménez-Vicente, J., Mediavilla, E., Muñoz, J. A., & Kochanek, C. S. 2012, *ApJ*, 751, 106
- Jiménez-Vicente, J. et al. 2013, in preparation
- Kuehn, C. A., Baldwin, J. A., Peterson, B. M., & Korista, K. T. 2008, *ApJ*, 673, 69
- Kuraszkiewicz, J. K., Green, P. J., Forster, K., Aldcroft, T. L., Evans, I. N. & Koratkar, A., 2002 *ApJ*, 143, 257
- Maoz, D., Netzer, H., Peterson, B. M., et al. 1993, *ApJ*, 404, 576
- Mediavilla, E., Muñoz, J. A., Kochanek, C. S., et al. 2005, *ApJ*, 619, 749
- Mediavilla, E., Muñoz, J. A., Lopez, P., et al. 2006, *ApJ*, 653, 942
- Mediavilla, E., Muñoz, J. A., Falco, E., et al. 2009, *ApJ*, 706, 1451
- Mediavilla, E., Muñoz, J. A., Kochanek, C. S., et al. 2011a, *ApJ*, 730, 16

- Mediavilla, E., Mediavilla, T., Muñoz, J. A., et al. 2011b, ApJ, 741, 42
- Morgan, C. W., Kochanek, C. S., Dai, X., Morgan, N. D., & Falco, E. E. 2008, ApJ, 689, 755
- Morgan, C. W., Kochanek, C. S., Morgan, N. D., & Falco, E. E. 2010, ApJ, 712, 1129
- Morgan, C. W., Hainline, L. J., Chen, B., et al. 2012, ApJ, 756, 52
- Mosquera, A. M., Kochanek, C. S., Chen, B., et al. 2013, ApJ, 769, 53
- Motta, V., Mediavilla, E., Muñoz, J. A., et al. 2002, ApJ, 574, 719
- Motta, V., Mediavilla, E., Falco, E., Muñoz, J. A. , 2012, ApJ, 755, 82
- Pooley, D., Blackburne, J. A., Rappaport, S., & Schechter, P. L. 2007, ApJ, 661, 19
- Pooley, D., Rappaport, S., Blackburne, J., et al. 2009, ApJ, 697, 1892
- Pooley, D., Rappaport, S., Blackburne, J. A., Schechter, P. L., & Wambsganss, J. 2012, ApJ, 744, 111
- Sluse, D., Claeskens, J.-F., Hutsemékers, D., & Surdej, J. 2007, A&A, 468, 885
- Sluse, D., Hutsemékers, D., Courbin, F., Meylan, G., & Wambsganss, J. 2012, A&A, 544, A62
- Vanden Berk, D. E., Richards, G. T., Bauer, A., et al. 2001, AJ, 122, 549
- Vestergaard, M., & Wilkes, B. J. 2001, ApJS, 134, 1
- Wambsganss, J. 2006, Saas-Fee Advanced Course 33: Gravitational Lensing: Strong, Weak and Micro, 453
- Zu, Y., Kochanek, C. S., & Peterson, B. M. 2011, ApJ, 735, 80



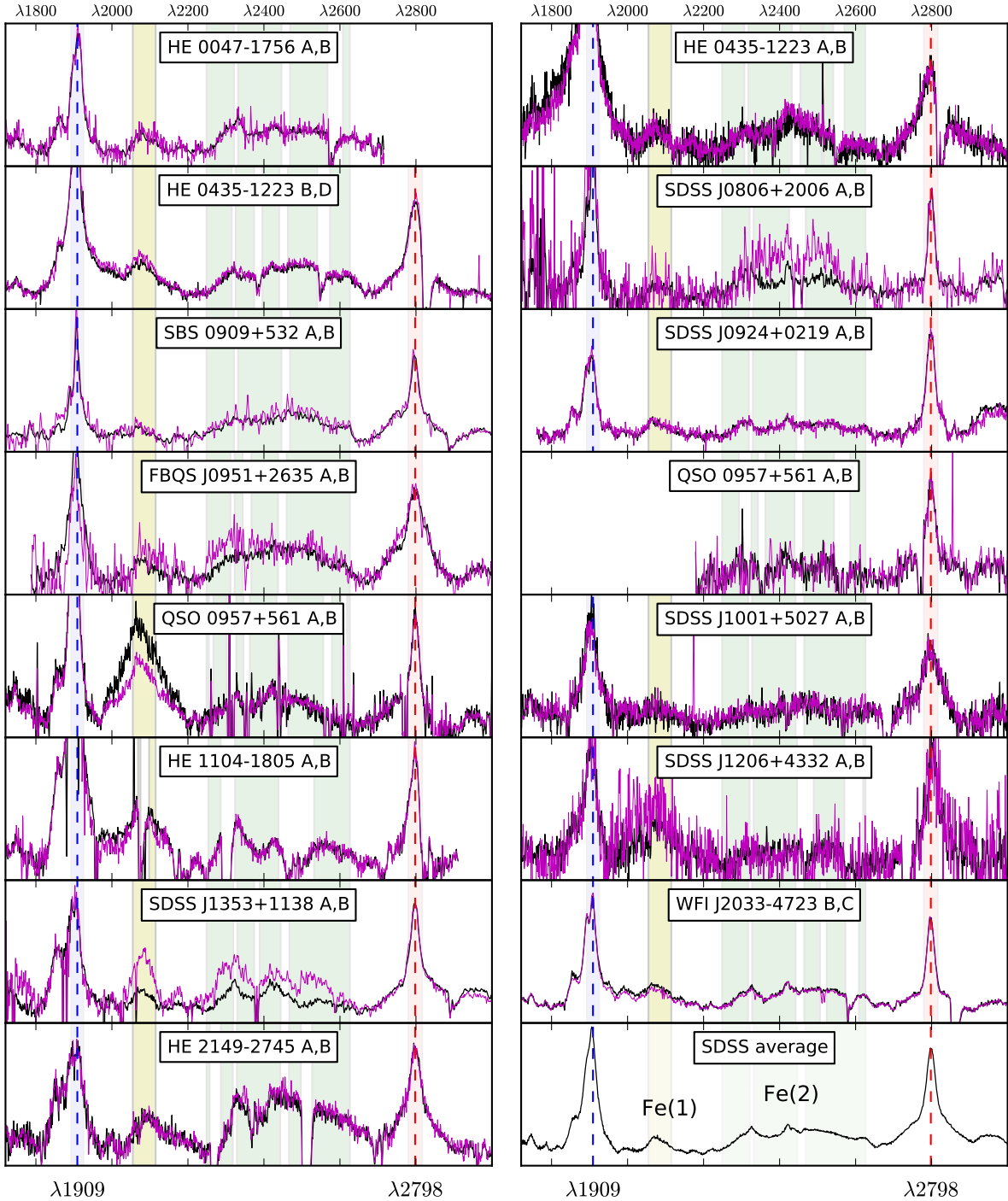


Fig. 1.— Panels showing superpositions of the paired spectra after continuum subtraction. The shaded regions show the wavelength intervals used for the C III]  $\lambda 1909$  line core, the Fe(1) blend, the Fe(2) blend and the Mg II  $\lambda 2798$  line core respectively (see Table 2). In the cases of SBS 0909+532 and SDSS J1353+1138 a linear model was used to correct for differential extinction between the images.

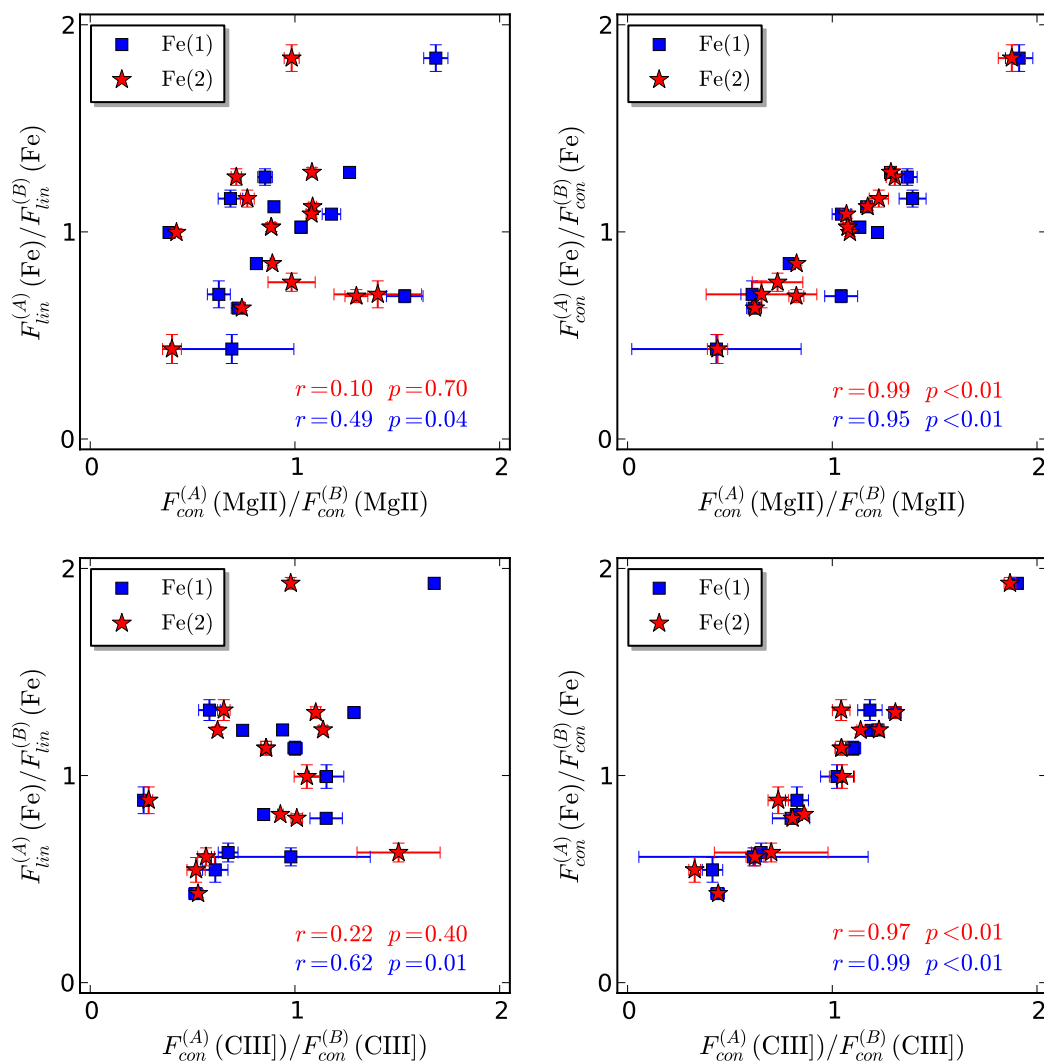


Fig. 2.— Comparison of Fe(1) and Fe(2) emission line and continuum flux ratios with the Mg II  $\lambda$ 2798 (top) and C III  $\lambda$ 1909 continuum ratios (bottom). Blue squares correspond to Fe(1) and red stars correspond to Fe(2).

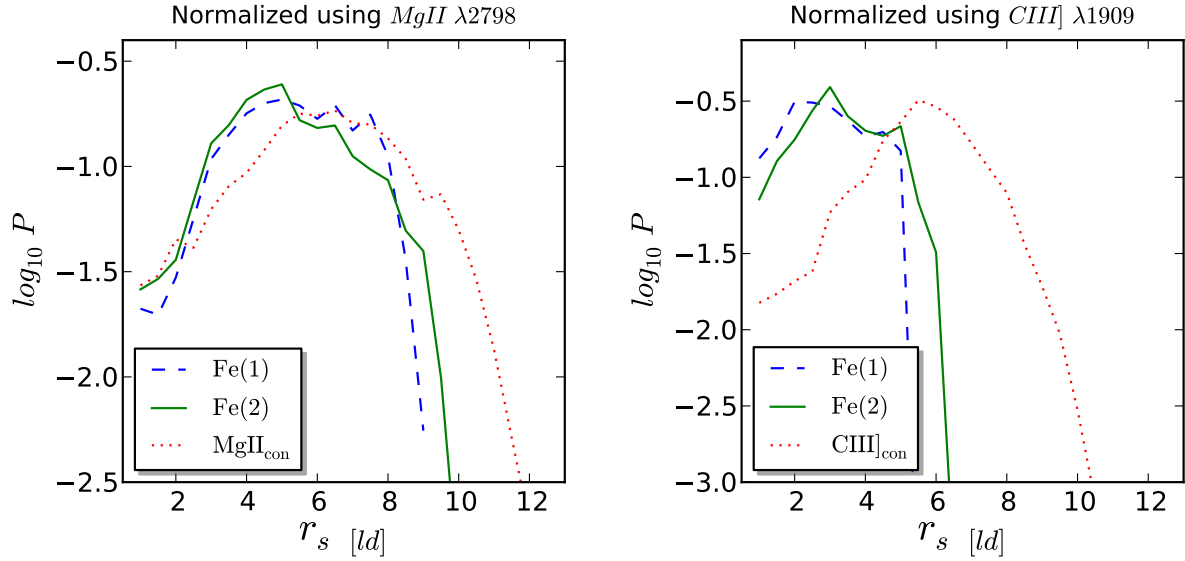


Fig. 3.— Posterior probabilities for a uniform prior on  $r_s$ . In the left (right) panel, the baseline for no microlensing magnification was set using the Mg II  $\lambda 2798$  (C III]  $\lambda 1909$ ) emission line. The dashed, solid and dotted curves correspond to Fe(1), Fe(2) and the continuum region associated with the normalizing line, Mg II  $\lambda 2798$  (left) or C III]  $\lambda 1909$  (right).

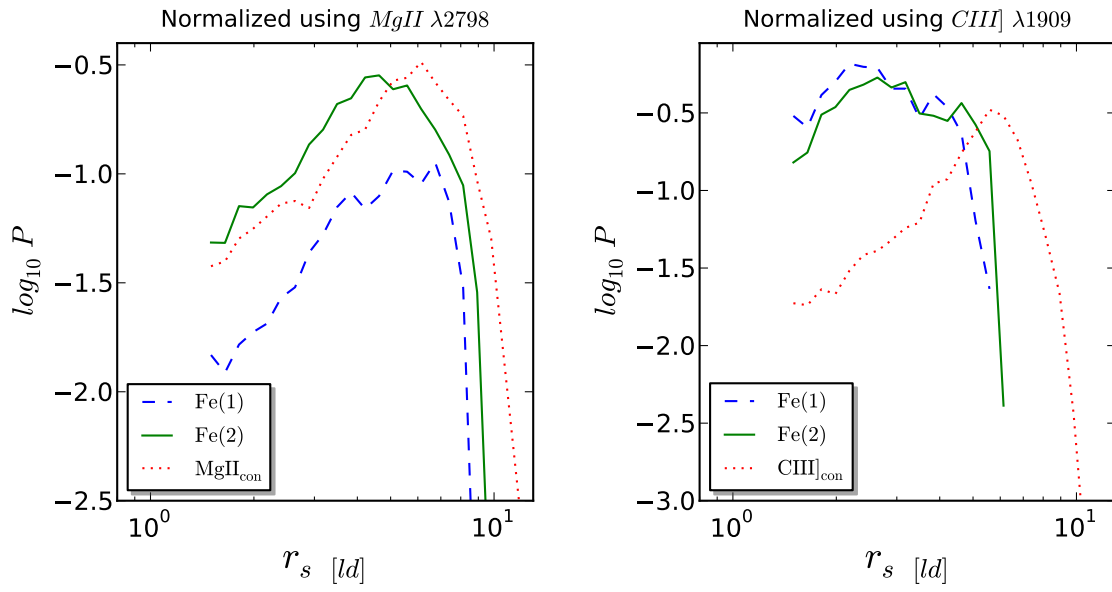


Fig. 4.— Same as Figure 3 but with a logarithmic prior on  $r_s$ .

Table 1. Summary of Data

Object (pair)	z	Observation Date	Rest wavelenght ( $\text{\AA}$ )	Reference
HE 0047–1756 A, B	1.67	2002 Sep 04	(1461 - 2547)	Wisotzki et al., 2004
HE 0435–1223 A, B	1.689	2008 Ene 12	(1210 - 3030)	Motta, V., unpublished data
HE 0435–1223 B, D	1.689	2004 Oct 12	(1638 - 2996)	Motta, V., unpublished data
SDSS 0806+2006 A, B	1.54	2005 Apr 12	(1575 - 3504)	Inada et al., 2006
SBS 0909+532 A, B	1.38	2003 Mar 07	(0750 - 5695)	Mediavilla et al., 2005
SDSS J0924+0219 A, B	1.524	2005 Jan 14	(1783 - 3170)	Eigenbrod et al., 2006
FBQ 0951+2635 A, B	1.24	1997 Feb 14	(1786 - 4018)	Schechter et al., 1998
QSO 0957+561 A	1.41	1999 Apr 15	(0913 - 4149)	Goicoechea et al., 2005
QSO 0957+561 B	1.41	2000 Jun 2-3	(0913 - 4149)	Goicoechea et al., 2005
QSO 0957+561 A, B	1.41	2008 Ene 13	(1330 - 3380)	Motta et al., 2012
SDSS J1001+5027 A, B	1.838	2003 Nov 20	(1409 - 3136)	Oguri et al., 2005
HE 1104–1805 A, B	2.32	2008 Abr 07	(1310 - 2909)	Motta et al., 2012
SDSS J1206+4332 A, B	1.789	2004 Jun 21	(1362 - 3048)	Oguri et al., 2005
SDSS J1353+1138 A, B	1.629	2005 Apr 12	(1521 - 3385)	Inada et al., 2006
WFI J2033–4723 B, C	1.66	2008 Abr 14	(1620 - 3625)	Motta, V., unpublished data
HE 2149–2745 A, B	2.033	2000 Nov 19	(1430 - 3174)	Motta, V., unpublished data

Table 2. Wavelength regions

Feature	Wavelength intervals (Å)	Description
Fe(1)	( $\lambda 2050^1$ , $\lambda 2115$ )	
Fe(2)	( $\lambda 2250$ , $\lambda 2320$ ) $\cup$ ( $\lambda 2333$ , $\lambda 2445$ ) $\cup$ ( $\lambda 2470$ , $\lambda 2625$ )	
Continuum	( $\lambda 2000$ , $\lambda 2020$ ) <sup>2</sup>	Bluewards of Fe(1)
Continuum	( $\lambda 2160$ , $\lambda 2180$ ) <sup>3</sup>	Redwards of Fe(1)
Continuum	( $\lambda 2225$ , $\lambda 2250$ ) <sup>3</sup>	Bluewards of Fe(2)
Continuum	( $\lambda 2640$ , $\lambda 2650$ ) <sup>4</sup>	Redwards of Fe(2)
Mg II $\lambda 2798$	( $\lambda 2776$ , $\lambda 2820$ )	Line core
C III] $\lambda 1909$	( $\lambda 1893$ , $\lambda 1925$ )	Line core

<sup>1</sup>Originally taken at  $\lambda 1942$  in Vestergaard et al. (2001).

<sup>2</sup>Contaminated with the wing of the C III] $\lambda 1909$  line (Kuraszkiewicz et al. 2002).

<sup>3</sup>Pure continuum window according to Kuraszkiewicz et al. (2002).

<sup>4</sup>As suggested in Francis et al. (1991). This continuum window is defined out of the Mg II $\lambda 2798$  wings (Brotherton et al. 2001) and of the iron blend Fe(2).

Table 3. Differential microlensing using Mg II $\lambda$ 2798 as reference.

Object (pair)	Fe(1) region	Fe(2) region	$\lambda$ 2798 continuum
HE 0435–1223 (B-A)	$+0.17^{+0.05}_{-0.04}$	$+0.37^{+0.04}_{-0.04}$	$-0.26^{+0.03}_{-0.03}$
HE 0435–1223 (D-B)	$+0.23^{+0.01}_{-0.01}$	$+0.13^{+0.01}_{-0.01}$	$+0.18^{+0.01}_{-0.01}$
SDSS J0806+2006 (B-A)	$+0.40^{+0.63}_{-0.39}$	$+1.00^{+0.13}_{-0.12}$	$+0.91^{+0.19}_{-0.16}$
SBS 0909+532 (B-A)	$-0.47^{+0.07}_{-0.06}$	$-0.29^{+0.05}_{-0.05}$	$+0.40^{+0.05}_{-0.05}$
SDSS J0924+0219 (B-A)	$+0.12^{+0.02}_{-0.02}$	$-0.09^{+0.02}_{-0.02}$	$-0.12^{+0.02}_{-0.02}$
FBQS J0951+2635 (B-A)	$+0.35^{+0.05}_{-0.05}$	$+0.33^{+0.02}_{-0.02}$	$+0.50^{+0.02}_{-0.02}$
QSO 0957+561 (B-A)	—	$+0.02^{+0.14}_{-0.12}$	$+0.30^{+0.06}_{-0.06}$
QSO 0957+561 (B-A)	$-0.57^{+0.04}_{-0.04}$	$+0.02^{+0.04}_{-0.04}$	$-0.66^{+0.04}_{-0.04}$
SDSS J1001+5027 (B-A)	$+0.41^{+0.10}_{-0.09}$	$+0.29^{+0.05}_{-0.05}$	$-0.16^{+0.04}_{-0.04}$
HE 1104–1805 (B-A)	$-0.18^{+0.04}_{-0.04}$	$-0.08^{+0.03}_{-0.03}$	$-0.09^{+0.02}_{-0.02}$
SDSS J1206+4332 (A-B)	$+0.50^{+0.10}_{-0.09}$	$-0.37^{+0.18}_{-0.15}$	$+0.39^{+0.11}_{-0.10}$
SDSS J1353+1138 (A-B)	$+1.04^{+0.03}_{-0.03}$	$+0.94^{+0.02}_{-0.02}$	$+0.00^{+0.02}_{-0.02}$
WFI J2033–4723 (B-C)	$-0.26^{+0.02}_{-0.02}$	$-0.09^{+0.02}_{-0.02}$	$-0.27^{+0.02}_{-0.02}$
HE 2149–2745 (B-A)	$-0.03^{+0.03}_{-0.03}$	$+0.13^{+0.02}_{-0.02}$	$-0.02^{+0.02}_{-0.02}$

Note. —  $\Delta m - \Delta m_{\text{MgII}\lambda 2798}$ , of the Fe(1) and Fe(2) blends after continuum subtraction, and of the Mg II $\lambda$ 2798 continuum. The Mg II $\lambda$ 2798 emission line flux (after continuum subtraction) is used as the no microlensing reference in all cases.

Table 4. Differential microlensing using C III] $\lambda$ 1909 as reference.

Object (pair)	Fe(1) region	Fe(2) region	$\lambda$ 1909 continuum
HE 0047–1756 (B-A)	$-0.15^{+0.08}_{-0.07}$	$-0.01^{+0.03}_{-0.03}$	$+0.25^{+0.03}_{-0.03}$
HE 0435–1223 (B-A)	$+0.32^{+0.03}_{-0.03}$	$+0.52^{+0.02}_{-0.02}$	$-0.21^{+0.02}_{-0.02}$
HE 0435–1223 (D-B)	$+0.18^{+0.02}_{-0.02}$	$+0.08^{+0.02}_{-0.02}$	$+0.23^{+0.02}_{-0.02}$
SDSS J0806+2006 (B-A)	$+0.02^{+0.55}_{-0.36}$	$+0.62^{+0.08}_{-0.08}$	$+0.54^{+0.08}_{-0.07}$
SBS 0909+532 (B-A)	$+0.54^{+0.12}_{-0.10}$	$+0.72^{+0.10}_{-0.09}$	$+0.66^{+0.13}_{-0.11}$
SDSS J0924+0219 (B-A)	$+0.07^{+0.02}_{-0.02}$	$-0.14^{+0.02}_{-0.02}$	$-0.22^{+0.02}_{-0.02}$
FBQS J0951+2635 (B-A)	$+0.72^{+0.07}_{-0.07}$	$+0.70^{+0.04}_{-0.04}$	$+0.92^{+0.05}_{-0.04}$
QSO 0957+561 (B-A)	$-0.56^{+0.02}_{-0.02}$	$+0.02^{+0.02}_{-0.02}$	$-0.71^{+0.02}_{-0.02}$
SDSS J1001+5027 (B-A)	$+0.59^{+0.10}_{-0.09}$	$+0.46^{+0.05}_{-0.05}$	$-0.30^{+0.04}_{-0.04}$
HE 1104–1805 (B-A)	$-0.16^{+0.08}_{-0.08}$	$-0.06^{+0.07}_{-0.06}$	$+0.01^{+0.06}_{-0.06}$
SDSS J1206+4332 (A-B)	$+0.43^{+0.08}_{-0.08}$	$-0.44^{+0.16}_{-0.14}$	$+0.50^{+0.08}_{-0.08}$
SDSS J1353+1138 (A-B)	$+1.46^{+0.08}_{-0.08}$	$+1.36^{+0.08}_{-0.07}$	$+0.14^{+0.08}_{-0.08}$
WFI J2033–4723 (B-C)	$-0.28^{+0.02}_{-0.02}$	$-0.11^{+0.02}_{-0.02}$	$-0.29^{+0.02}_{-0.02}$
HE 2149–2745 (B-A)	$+0.00^{+0.04}_{-0.04}$	$+0.16^{+0.03}_{-0.03}$	$-0.13^{+0.03}_{-0.03}$

Note. —  $\Delta m - \Delta m_{\text{CIII}\lambda 1909}$ , of the Fe(1) and Fe(2) features after continuum subtraction, and of the C III] $\lambda$ 1909 continuum. The C III] $\lambda$ 1909 emission line flux (after continuum subtraction) is used as the no microlensing reference in all cases.